

Underwater Hyperspectral Imaging Using a Stationary Platform in the Trans-Atlantic Geotraverse Hydrothermal Field

Ines Dumke^{ID}, Martin Ludvigsen, Steinar L. Ellefmo, Fredrik Søreide, Geir Johnsen, and Bramley J. Murton

Abstract—Underwater hyperspectral imaging is a relatively new method for characterizing seafloor composition. To date, it has been deployed from moving underwater vehicles, such as remotely operated vehicles and autonomous underwater vehicles. While moving vehicles allow relatively rapid surveying of several 10–1000 m², they are subjected to short-term variations in vehicle attitude that often compromise image acquisition and quality. In this study, we tested a stationary platform that was landed on the seabed and used an underwater hyperspectral imager (UHI) on a vertical swinging bracket. The imaged seafloor areas have dimensions of 2.3 m × 1 m and are characterized by very stable UHI data of high spatial resolution. The study area was the Trans-Atlantic Geotraverse hydrothermal field at the Mid-Atlantic Ridge (26° N) in water depths of 3530–3660 m. UHI data were acquired at 12 stations on an active and an inactive hydrothermal sulfide mound. Based on supervised classification, 24 spectrally different seafloor materials were detected, including hydrothermal and non-hydrothermal materials, and benthic fauna. The results show that the UHI data are able to spectrally distinguish different types of surface materials and benthic fauna in hydrothermal areas, and may therefore represent a promising tool for high-resolution seafloor exploration in potential future deep-sea mining areas.

Index Terms—Image classification, remote sensing, spectroscopy, terrain mapping, underwater object detection.

I. INTRODUCTION

HYPERSPECTRAL imaging is defined as the acquisition of image data over hundreds of narrow, contiguous spectral bands [1]. Each image pixel contains a full spectrum of dif-

Manuscript received October 21, 2017; revised March 12, 2018 and August 13, 2018; accepted October 27, 2018. Date of publication December 24, 2018; date of current version April 22, 2019. This work was supported in part by the European Union's Seventh Framework Program for research, technological development and demonstration through the Blue Mining project under Grant 604500 and in part by the Norwegian Research Council through the NTNU AMOS Centre of Excellence under Grant 223254. (*Corresponding author: Ines Dumke.*)

I. Dumke was with the Department of Marine Technology, Norwegian University of Science and Technology, 7491 Trondheim, Norway. She is now with the GEOMAR Helmholtz Centre for Ocean Research Kiel, 24148 Kiel, Germany (e-mail: idumke@geomar.de).

M. Ludvigsen and F. Søreide are with the Department of Marine Technology, Norwegian University of Science and Technology, 7491 Trondheim, Norway.

S. L. Ellefmo is with the Department of Geoscience and Petroleum, Norwegian University of Science and Technology, 7491 Trondheim, Norway.

G. Johnsen is with the Department of Biology, Centre for Autonomous Marine Operations and Systems, Norwegian University of Science and Technology, 7491 Trondheim, Norway.

B. J. Murton is with the National Oceanography Centre, Southampton SO14 3ZH, U.K.

Color versions of one or more of the figures in this paper are available online at <http://ieeexplore.ieee.org>.

Digital Object Identifier 10.1109/TGRS.2018.2878923

ferent spectral components comprising information about the surface material (soil/rock), biology (vegetation/encrustation), atmosphere/water, as well as the properties of the illumination source and geometry, and the imager [1], [2]. To obtain a reflectance spectrum specific for a particular material or object of interest (OOI), calibrations correcting for all external influences are required [3], [4]. The reflectance spectrum represents the percentage of light that is reflected off the OOI at each wavelength.

Different OOIs can be discriminated based on their characteristic reflectance spectra (optical fingerprints), allowing characterization of OOIs through spectral classification. In spectral classification, each image pixel spectrum is compared to a set of known endmember spectra, e.g., from a spectral library or field samples, to find the best matching endmember spectrum and identify OOIs [3], [5]. Spectral classification results are generally output as coverage maps showing the distribution of different OOIs in a given area.

For subaerial purposes, hyperspectral data are typically acquired by hyperspectral imagers on airplanes or satellites. These hyperspectral imagers are passive imagers as they use the sun as a light source for surface illumination. They record the intensity of reflected solar radiation over a wavelength range of 400–2500 nm [2], [6], [7] and are used in both onshore and offshore settings.

Subaerial hyperspectral studies are conducted for different purposes, including the mapping of vegetation [8], [9] and infrastructure [10], [11]. An important application is mapping surface minerals and soils to detect ore deposits for mineral exploration [2], [6], [7], [12], [13]. As many minerals are associated with characteristic absorption spectra in the near-infrared and infrared parts of the solar spectrum [14], hyperspectral imaging provides useful information on surface composition in potential mining areas [6], [15].

Passive airborne and spaceborne hyperspectral imagers have also been used in offshore settings to map and characterize seafloor habitats, e.g., seagrass and kelp habitats and coral reefs [16]–[20]. However, due to the attenuation of specific wavelengths and intensity with depth, these applications were limited to shallow waters (<20 m depth) and nonturbid (clear) coastal fringes.

To enable hyperspectral seafloor imaging surveys in deeper waters with no natural light penetration, active underwater hyperspectral imagers (UHIs) such as the UHIs by Ecotone AS, Trondheim, Norway [21], [22], have been developed over

the past eight years. These imagers are combined with external light sources for seafloor illumination and can be deployed in water depths of up to 6000 m [21]–[26]. Given the strong in-water attenuation of near-infrared and infrared wavelengths, the UHIs mostly cover the visible range of wavelengths at high spectral (up to 0.5 nm) and spatial resolutions (millimeter-centimeter range).

UHIs are typically deployed on remotely operated vehicles (ROVs) that are operated in close proximity (a few meters) to the seafloor [23]–[26] to account for the range and wavelength dependent attenuation of light in seawater. Recently, a UHI was also used on an autonomous underwater vehicle (AUV) [28]. Moving UHI platforms allow mapping of larger seafloor areas, but they are also subjected to vehicle motion and variations in pitch, roll, and altitude, which influence the UHI measurements and may compromise data quality. Remotely operated stationary platforms might provide more stable UHI data, but so far, stationary UHI measurements have not been conducted, except for SCUBA-based UHI surveys using a UHI on a tripod in shallow waters [25].

Previous UHI surveys mainly focused on biological mapping, e.g., at cold-water coral reefs and kelp forests [24], [25]. However, the UHI method is also suitable for mapping and characterizing geological seafloor materials [23] and was recently applied to image manganese nodules in 4200 m water depth [26]. These results indicate that UHIs are able to spectrally distinguish different types of geological materials, despite the limitation to the visible range of the solar spectrum. Underwater hyperspectral imaging may therefore be a promising method for high-resolution mapping and classification of seafloor materials in areas considered for potential future seabed mining operations. Aside from manganese nodules, current targets for seabed resource exploitation are seafloor massive sulfide (SMS) deposits in hydrothermal areas [29]–[33].

SMS deposits are typically found at plate boundaries, and in particular along the mid-ocean ridges [34], [35]. There are over 350 known examples, including the Atlantis II Deep in the Red Sea [36], the East Pacific Rise near 21° N [37], and several areas along the Mid-Atlantic Ridge, such as the Ashadze (13° N) and Krasnov (16° N) hydrothermal fields [38], the Trans-Atlantic Geotraverse (TAG) hydrothermal field at 26° N [39]–[43], and the Loki's Castle vent field at 73° N [44]. At these locations, mineral deposits form at and beneath the seafloor through precipitation from hydrothermal fluids during contact with cooler seawater. SMS are predominantly composed of sulfide minerals rich in base metals (Cu, Fe, Zn, and Pb), but may also contain Ag and Au [34], [41], [42]. Due to their mineral composition, SMS are regarded as an important potential resource for exploitation [29]–[31].

Exploitation of SMS is not yet an active industry, but is predicted to start within the next few years in the Bismarck Sea, Papua New Guinea, where Nautilus Minerals has been granted the first exploitation license for SMS [45]. Prior to exploitation, extensive exploration is required, including high-resolution mapping and characterization of both the seafloor and the subsurface. Seafloor exploration surveys at high spatial resolution are also important for environmental

management in potential mining areas to understand and mitigate the impact of future mining operations on hydrothermal ecosystems [46]–[50].

Here, we present high-resolution active hyperspectral image data from the seafloor at two hydrothermal SMS mounds located in the TAG hydrothermal field at the Mid-Atlantic Ridge (26° N). We report the first use of a UHI scanning unit on a stationary platform (the Hydraulic Benthic Interactive Sampler system—HyBIS) in deep (3600 m) water. The acquisition system is evaluated for performance and data quality, and recommendations for future UHI surveys are given. Supervised classification is performed to analyze abundance and distribution of spectrally different materials, and a preliminary spectral library is created for the TAG area.

II. TAG HYDROTHERMAL FIELD

The TAG hydrothermal field is located on the Mid-Atlantic Ridge between 26° 8'N and 26° 10'N [Fig. 1(a)] and has been studied intensively since its discovery in 1985 [39]–[42], [51], [52]. With an area of approximately 5 km × 5 km, it is one of the largest known submarine hydrothermal fields and comprises both active and inactive sulfide deposits in water depths of 3400–3700 m.

The best studied deposit is the TAG Mound [Fig. 1(c)], a hydrothermally active sulfide mound approximately 250 m in diameter and 45 m high, which is composed largely of massive sulfides (pyrite, chalcopyrite, and sphalerite) often cemented by anhydrite [40], [51], [55]. Hydrothermal fluids with temperatures of up to 366 °C are discharged from a black smoker complex at the top of the mound. Radiometric dating of hydrothermal deposits indicated an evolution over at least 140 000 years, characterized by recurring phases of high-temperature activity, the most recent of which may have begun about 80 years ago [56].

In addition to the active TAG Mound, several inactive sulfide deposits exist in the area. These deposits include the elongated MIR zone (0.7 km × 1 km) and several sulfide mounds comparable in size to the TAG Mound, namely, Southern Mound [Fig. 1(b)], Shinkai Mound, Alvin Mound (also known as Double Mound), and Shimmering Mound. The mounds have diameters of approximately 150–200 m and are partially covered by pelagic sediments, with discontinuous outcrops of sulfides and relict chimneys [40], [41]. Recent new high-resolution (0.5 m²) bathymetric data also reveal the presence of additional smaller sulfide mounds in the TAG field [54].

III. METHODS

A. Data Acquisition

1) *UHI Surveys*: Hyperspectral data were acquired in the TAG hydrothermal field in 2016 during the Blue Mining cruise JC138 onboard the RRS James Cook. Survey stations were chosen based on a relatively flat bathymetry that allowed safe landing of the HyBIS robotic underwater vehicle (RUVE), and the presence of potentially hydrothermal material as inferred from the HyBIS video feed. For comparison purposes, non-hydrothermal material, including seabed fauna, was also targeted. Two UHI surveys were conducted, one in the area of the

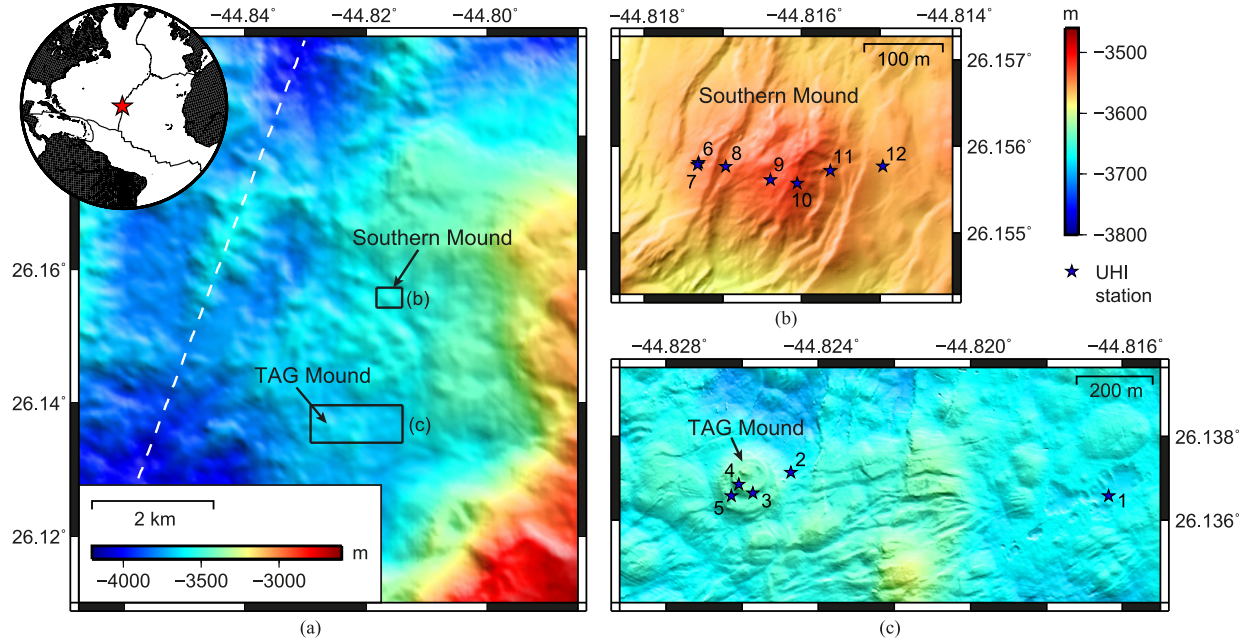


Fig. 1. Overview of the study area. (a) Ship-based bathymetry (30 m resolution) showing the TAG hydrothermal field (location marked in the inset) with the study areas TAG Mound and Southern Mound. The white dashed line indicates the ridge center. Plate boundaries are from [51]. (b) UHI stations at Southern Mound (second survey). (c) UHI stations at and around TAG Mound (first survey). The high-resolution bathymetry (0.5–2 m resolution) shown in (b) and (c) was collected by the AUV Abyss (GEOMAR) during RV Meteor cruise M127 in 2016 [54]. Note that the color scale in (a) differs from that in (b) and (c).

active TAG Mound and one at the inactive Southern Mound. In total, data were recorded at 12 stations, located inside a former lava lake pit 900 m east of TAG Mound (station 1), close to or on TAG Mound (stations 2–5), on the western flank of Southern Mound (stations 6–7), on Southern Mound (stations 8–11), and in a gully east of Southern Mound (station 12) [Fig. 1(b) and (c)]. Water depths at the stations were about 3638–3655 m for the TAG survey (stations 1–5) and 3530–3561 m for the Southern Mound survey (stations 6–12).

2) *Underwater Hyperspectral Imager*: Hyperspectral image data were acquired using a UHI depth-rated to 6000 m, which was developed by Ecotone AS (Trondheim, Norway) [21], [22]. The UHI consists of a fore lens (8 mm), a spectrograph, and a light-sensitive sCMOS camera in an underwater steel housing [25], [26]. It is a push-broom scanner with beamwidths of 60° (transverse) and 0.4° (longitudinal) and is mounted looking vertically downward [Fig. 2(b)]. Hyperspectral data are recorded for a line of 1600 pixels perpendicular to the track direction. To acquire image data along a survey track, the UHI needs to be moved forward at a relatively constant speed (approximately 0.05 m·s⁻¹ [26]). Reflected light intensities can be measured for up to 896 spectral bands between 378 and 805 nm, with a spectral resolution of 0.5 nm. In this study, hyperspectral data were recorded at 30 Hz for 224 spectral bands with a spectral resolution of 2 nm.

3) *Acquisition Setup*: The HyBIS RUV [Fig. 2(a)] was used as the mounting platform for the UHI. Designed by Hydro-Lek (Finchampstead, U.K.) and the National Oceanography Centre (Southampton, U.K.), HyBIS is a remotely operated underwater platform that can be deployed down to 6000 m water depth. It is typically used for seafloor video surveys and sampling,

and provides a versatile alternative to a conventional ROV, the main difference being that HyBIS lacks any floatation and is subjected directly to the ship's motion via the umbilical cable [57]. Positioning information was provided by a Sonardeyne ultra-short baseline (USBL) transponder.

Although HyBIS can be moved via its thrusters, it acted as a lander in this study and was stationary on the seafloor during UHI measurements. The UHI was mounted on a vertical swinging bracket attached to the front of the HyBIS frame and actuated by a hydraulic ram [Fig. 2(a) and (b)]. The UHI's viewing slit of 1600 pixels was oriented perpendicular to the HyBIS frontal frame. Forward motion of the UHI was achieved by swinging the UHI 40° (from vertical) to HyBIS port and starboard [Fig. 2(b)] and thus simulating a survey track covering an area of approximately 2.3 m × 1 m in front of HyBIS. The central altitude of 0.97 m (swinging angle of 0°) resulted in a resolution of 0.7 mm per image pixel; at the track ends (swinging angle of ±40°), the resolution was 1 mm per pixel.

Seafloor illumination was provided by two halogen lamps (Deep Multi-SeaLite, 250 W each) mounted at a fixed distance of 23 cm from the UHI's center [Fig. 2(a) and (b)]. The lamps were slightly angled toward the UHI (about 5°) to ensure overlap of their light cones beneath the UHI. As the lamps could only be mounted in front of and behind the UHI, rather than on either side, seafloor illumination was best in the center of the surveyed track. All other HyBIS lamps were turned off during UHI data acquisition.

B. Data Processing

The raw UHI data were influenced by several factors, including the seafloor material, illumination, the inherent

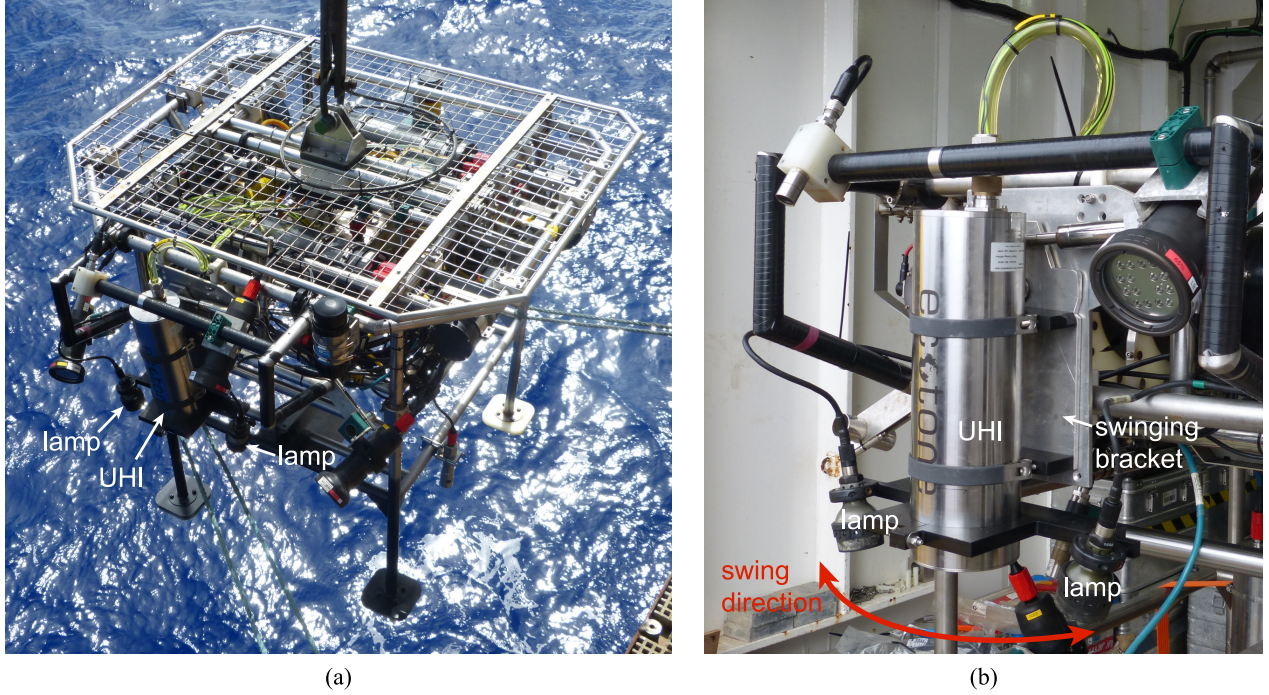


Fig. 2. (a) HyBIS with the UHI mounted at the front. (b) The UHI was mounted on a vertical, hydraulically actuated swinging bracket that swung the UHI in an 80° arc (from -40° to 40°) to allow surveying along a 2.3-m-long track. Two halogen lamps attached on either side of the UHI provided seafloor illumination.

optical properties of the water column, UHI altitude and swinging angle, and the sensor itself. The aim of the data processing was to correct for all external influences and obtain reflectance data with spectral responses specific for the seafloor material. Processing of the UHI data was done using a combination of the Hypermap software (Ecotone) and MATLAB (Mathworks). The following processing steps were applied: 1) calibration of the raw data (digital counts) to radiance data (in $\text{W}\cdot\text{m}^{-2}\cdot\text{sr}^{-1}\cdot\text{nm}^{-1}$); 2) calibration of radiance data to reflectance data; and 3) geocorrection.

1) Calibration to Radiance Data and Subsetting: Calibration of the raw UHI data to radiance data removed sensor-specific influences through radiometric correction and was done using the Hypermap software. Following radiance calibration, spatial subsetting of the data was performed to remove redundant information at the track ends where the UHI was not yet or no longer moving, but still recording. It was also necessary to cut off a 15–20 cm wide part of the track containing part of the lower HyBIS frame, which was in the field of view of the UHI. In addition, spectral subsetting was applied to remove noisy outer bands and reduce the data to 174 spectral bands between 400 and 730 nm. The spectral resolution (2 nm) was not affected by this step.

2) Calibration to (Pseudo) Reflectance: Calibration of radiance to reflectance data involves the removal of influences from illumination, inherent optical properties of the water column, and acquisition geometry, so that the spectral responses depend only on the seafloor material. To correct for illumination influences, an illumination reference is required that describes the spectral characteristics of the illumination conditions during data acquisition for the wavelength range used (378–805 nm). The illumination reference may be

obtained from a Spectralon reference standard [23], [25], [58] or from a combination of light intensity measurements under different angles and radiative transfer modeling [23], but it can also be approximated from the radiance data [26].

To obtain an illumination reference directly from the radiance data and correct for illumination influences, we developed a MATLAB-based approach in which the spectral intensities stored in each pixel spectrum were first normalized along the track to the level of the central altitude (UHI in vertical position). This step removed illumination influences related to along-track changes in distance to the seafloor, which was due to the change of the swinging angle and the associated slant range. The pixel spectra were then corrected in across-track direction via along-track median spectra, a procedure that had been successful in correcting across-track illumination variations in a previous data set acquired with the same UHI [26]. Further details are given in Section III-B2a and III-B2b. We assumed that this approach also corrected for influences from water column properties, which were unknown for all UHI stations but were assumed to be constant during the period of study at each site.

a) Along-track intensity normalization: Intensity normalization was performed in MATLAB, which treats hyperspectral data as a spectral cube, i.e., a 3-D array $A(m, n, i)$ of m lines (the number of lines along the track), n samples (the number of pixels of the UHI slit, or across the track), and i spectral bands. While the number of recorded spectral bands and samples was constant for all tracks (174 spectral bands and 1598 samples), the number of lines varied between 420 and 770 (on average 584). The following calculations are all based on this data structure.

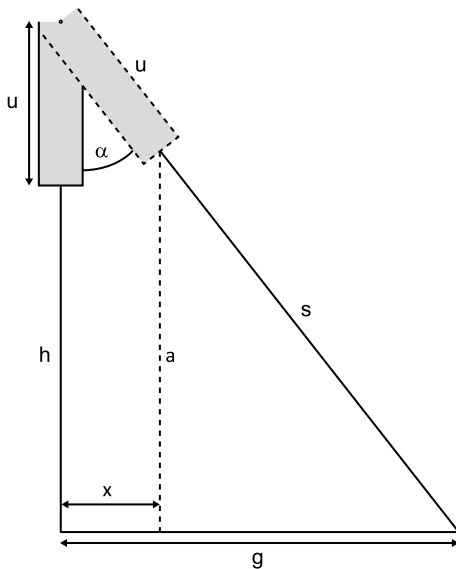


Fig. 3. Schematic for the acquisition geometry. α = swinging angle, u = distance from UHI lens to UHI pivot, h = central altitude (UHI in vertical position), a = altitude, s = slant range, g = ground range, and x = horizontal distance between UHI lens and central position.

For intensity normalization, the swinging angle and the slant range needed to be known. The swinging angle was not recorded along the track, and therefore had to be approximated from the acquisition geometry. To calculate the swinging angle and slant range, the following assumptions were made: 1) the rate of change of the swinging angle was constant along the track; 2) each track represented a full 80° swing from -40° to $+40^\circ$; and 3) the seafloor was flat relative to HyBIS.

For each line m along a survey track, the swinging angle α was calculated as

$$\alpha(m) = (m - 1)\Delta\alpha - 40^\circ \quad (1)$$

where $\Delta\alpha$ corresponds to the angle interval between two consecutive lines m , assuming a constant rate of change of α and a full 80° swing:

$$\Delta\alpha = \frac{80^\circ}{m_{\text{total}}} \quad (2)$$

where 80° corresponds to a full swing from -40° to $+40^\circ$ from vertical and m_{total} is the number of lines along the survey track. Each angle $\alpha(m)$ was associated with a slant range $s(m)$, which is the distance between UHI lens and seafloor along the light path (Fig. 3). Using the trigonometric relationship

$$\cos \alpha(m) = \frac{h + u}{s(m) + u} \quad (3)$$

where $h = 0.97$ m is the central altitude or minimum slant range (UHI in vertical position) and $u = 0.4$ m is the distance between UHI lens and pivot (Fig. 3), the slant range was calculated as

$$s(m) = \frac{h + u}{\cos \alpha(m)} - u. \quad (4)$$

The path length of the reflected light was simplified as $2s$ by assuming that the light was issued from and reflected to

the same point (i.e., the UHI lens). Although the lamps were mounted at a distance of 23 cm outboard from the UHI, this assumption was regarded as true because the lamps were on the same level as the UHI lens and their light cones overlapped to ensure greatest illumination at the UHI lens. Based on this assumption, the radiance data were normalized to twice the central UHI altitude ($2h$)

$$\text{int}_{\text{norm}}(m, n, i) = \text{int}(m, n, i) \frac{2s(m)}{2h} \quad (5)$$

where $\text{int}(m, n, i)$ is the radiance intensity of the image pixel (m, n) for the spectral band i .

b) Across-track illumination corrections to obtain (pseudo) reflectance: To correct for across-track illumination differences, we used an approach that had worked well for illumination equalization in a previous study [26]. In the following, the notation S is used to describe a spectrum, i.e., a vector with a dimension equal to the number of spectral bands.

For each sample n along the UHI slit, a reference spectrum $S_{\text{ref}}(n)$ was calculated as the median spectrum of all normalized radiance spectra $S_{\text{norm}}(m, n)$ recorded for this sample n along the survey track. For each image pixel (m, n) , the normalized radiance spectrum was then divided by its respective reference spectrum

$$S_{\text{corr}}(m, n) = \frac{S_{\text{norm}}(m, n)}{S_{\text{ref}}(n)} \quad (6)$$

where $S_{\text{corr}}(m, n)$ is the corrected spectrum for image pixel (m, n) .

It is important to note that with this method of data processing, i.e., using median spectra as illumination reference, the processed data were not true reflectance. The applied method was able to correct for most of the illumination influences, but residual illumination effects, and possibly influences from water column properties, may remain. The processed data therefore represent pseudo-reflectance rather than true reflectance data [24]. Although it would generally be preferable to have true reflectance data, this is not necessary for spectral classification.

3) Geocorrection: Geocorrection, which included georeferencing and correction for the UHI attitude during acquisition, was done using the geocorrection tool of the Hypermap software. This tool required the input of a navigation file containing information on positioning and attitude during acquisition. When UHI data are acquired on an ROV, this information is obtained from the ROV navigation file. With acquisition on HyBIS, however, the HyBIS navigation file did not contain the necessary information, as only the UHI was moved along a survey track, while HyBIS remained stationary. An artificial navigation file was therefore created by calculating the required geometric parameters based on the HyBIS position and acquisition geometry.

For the navigation file, the UHI altitude and positioning (latitude and longitude) were calculated for each line m along the track based on the acquisition geometry shown in Fig. 3. Using the intercept theorem

$$\frac{a(m)}{s(m)} = \frac{h + u}{s(m) + u} \quad (7)$$

the UHI altitude $a(m)$ for each line m was calculated by

$$a(m) = s(m) \frac{h + u}{s(m) + u}. \quad (8)$$

The UHI position was then calculated from the central UHI position ($\alpha = 0$) and the horizontal distance $x(m)$ to this position. The central UHI position was determined from the known HyBIS position and the fixed distance between the UHI and the HyBIS USBL transponder. Applying the intercept theorem based on Fig. 3,

$$\frac{g(m)}{s(m) + u} = \frac{g(m) - x(m)}{s(m)} \quad (9)$$

where $g(m)$ represents the ground range and $x(m)$ the horizontal distance between the UHI lens and the central position in the swinging direction. The ground range $g(m)$ for each line m was calculated as

$$g(m) = (s(m) + u) \sin \alpha(m) \quad (10)$$

Solving (9) for $x(m)$ results in

$$x(m) = g(m) \left(1 - \frac{s(m)}{s(m) + u} \right). \quad (11)$$

Based on the distance $x(m)$ and the UHI's central position, the UHI position for each line m was then calculated via MATLAB'S reckon function. After entering altitude and positioning information into the navigation file, geocorrection was performed and the data were output with a pixel size of 1 mm.

After georeferencing, the areas imaged at each station were approximately 2.3 m in length, while the track width increased from 0.65–0.7 m at the center to 0.9–0.95 m at the track ends. Because of the acquisition method and associated changes in altitude and slant range along the track, the spatial resolution is highest in the center of the imaged area where the track was narrowest. The spatial resolution decreases toward both track ends and thus features at the track ends may appear slightly blurry.

C. Supervised Classification

Spectral classification was performed to distinguish and map spectrally different seafloor materials. A standard classification method, the support vector machine (SVM), was applied using the ENVI software (Exelis VIS). SVM separates spectral classes by decision surfaces or so-called hyperplanes that maximize the margin between the classes, while support vectors from training data define the points closest to the hyperplanes [59]–[62]. The method was chosen as it is often superior to other supervised classification methods [60], [63], even for noisy and complex data [59]. SVM also provided good classification results in a previous study using the same UHI [26].

Training data for the classification were obtained from the UHI data via user-defined regions of interest (ROIs) that represented spectrally different materials. The ROIs were defined manually based on visual differences in the UHI “pseudo”-RGB data, which was composed of the three spectral bands 620 (R), 550 (G), and 450 nm (B) (Fig. 4), as well

as visual comparisons of pixel spectra covering the range of 400–730 nm, and appearance in the HyBIS standard definition RGB video feed prior to landing on the seafloor. Using the ROIs, SVM was run to produce a first classification image. The ROIs were then improved by adding more pixels to account for spectral variability within potential material classes, and SVM was run again, which was repeated until the SVM output was satisfying. The SVM classification images were then smoothed via ENVI's classification aggregation tool, using a pixel threshold of five to merge smaller pixel clusters into the surrounding class.

Determining the accuracy of the SVM results was difficult due to the general lack of ground-truthing information. If ground-truthing images of the seafloor areas scanned by the UHI had been available, the classification accuracy could have been estimated on a pixel-by-pixel basis via a confusion matrix [64]. Although the HyBIS videos provided some ground-truthing information, video data were not acquired along the UHI tracks as the cameras pointed perpendicular to the UHI track direction. Therefore, the classification accuracy was estimated from visual comparisons of the SVM images and the UHI pseudo-RGB images.

To set up a first spectral library for the study area, mean spectra were calculated for the ROIs of each station. All mean spectra were then compared to find spectral similarities between spectra from different stations, which could indicate the presence of the same materials. Based on these comparisons, groups of similar ROI spectra were averaged and stored in a spectral library containing an endmember spectrum for each material class.

IV. RESULTS

A. Quality of Pseudo-reflectance Data

Good processing results were obtained for eight of the 12 stations: four stations in the TAG Mound area [stations 1–4; Fig. 1(c)] and four on Southern Mound [stations 6, 8, 9, and 11; Fig. 1(b)]. The data from these stations were characterized by very sharp images, especially in the central part of the track, as well as the absence of processing artifacts and distortions [Figs. 4 and 5(a)]. Illumination was relatively even both along and across the track, although some exceptions existed, such as brighter areas associated with elevated features. Only these eight stations were used for supervised classification and further analyses.

For stations 5, 7, and 10, the processing approach worked less well and resulted in some artifacts in the data. This may have been partly due to the illumination and landing conditions at these stations. For example, at station 5, HyBIS half perched on a rock while leaning 34° to port, and the resulting illumination differences along and across the track were likely too large to be corrected with the applied processing method. At station 12, mainly particles in the water column were imaged. This particle cloud was not apparent from the video feed during acquisition.

All stations exhibited shadows in the data, which mostly occurred at one or both track ends. At stations 1–5, these shadows were due to the housing of the starboard HyBIS

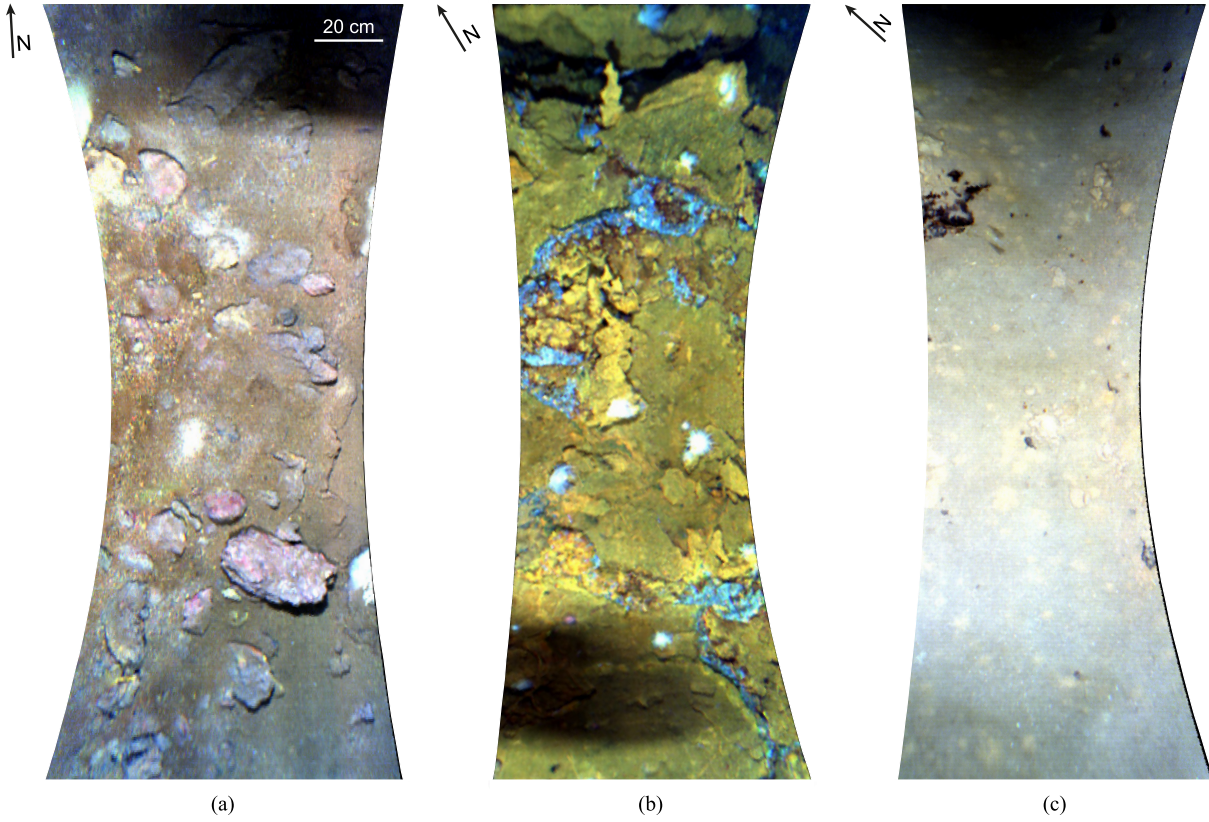


Fig. 4. Geocorrected pseudo-reflectance data in pseudo-RGB (R: 620 nm, G: 550 nm, and B: 450 nm). The scale is the same for all images. (a) Station 2 east of TAG Mound, showing brown-red sediment and potentially hydrothermal rocks with oxide staining. (b) Station 4 on TAG Mound, characterized by a rock platform with outcrops of atacamite, oxide staining, and anemones. (c) Station 6 on the western flank of Southern Mound, showing mostly pelagic sediment and dark crusts. The shadowed areas at the top of (a) and lower end of (b) were caused by the housing of the starboard HyBIS lamp. Station locations are shown in Fig. 1.

lamp. In addition, smaller shadows associated with small-scale topography were present within the images.

B. Seafloor Characteristics at the UHI Stations

The UHI data and video data from the 12 stations showed a variety of surface materials. Although the stations only represented point measurements, they revealed both differences and similarities between the active TAG Mound and the inactive Southern Mound.

At and around TAG Mound (stations 2–5), the seafloor was characterized by dark brown to brown–red sediments and oxide staining on both rocks and sediments [Figs. 4(a) and (b) and 5(a)]. Stations 2 and 3 exhibited multiple oxide-stained rocks [station 2, Fig. 4(a)] and relict chimneys [station 3, Fig. 5(a)]. Station 4 represented a rock platform with outcrops of atacamite [Fig. 4(b)]. Anemones found at stations 3 and 4 [Figs. 4(b) and 5(a)] were the only seabed fauna imaged by the UHI.

On Southern Mound, sediments were mostly lighter colored [Fig. 4(c)], but darker red sediments were present at stations 8 and 11. Oxide staining was observed at stations 8, 9, and 11. Pieces of dark crust were imaged at station 6 [Fig. 4(c)], and station 9 was characterized by yellow-brown bacterial mats. Although these mats were blown away completely when HyBIS landed on the seafloor, the sediment beneath them

had a strong signature in the UHI data. In addition, round patches of sediment that was slightly darker or lighter than the background sediment were observed at stations 6 and 7, and also at station 1 in the former lava lake pit. Station 1 was mostly characterized by light-colored pelagic sediment.

C. Classification Results

1) *SVM Results:* In total, 48 ROIs were defined for the eight stations used for spectral classification. The number of ROIs per station varied between four (station 9) and ten (station 3), with an average of six ROIs per station. Due to the presence of shadows in the data, shadows were included as a separate ROI for each station.

Overall, the UHI data of all eight stations seemed well classified by the SVM method. For example, the classification of atacamite at station 4 [Fig. 6(b)], the orange oxide staining at station 3 [Fig. 5(b)], the crust at station 6 [Fig. 6(c)], and the bulk part of the anemones [stations 3 and 4; Figs. 5(b) and 6(b)] appeared to be relatively accurate. However, there were also some exceptions where pixels may not have been classified correctly, e.g., the spicules of some anemones [Figs. 5(b) and 6(b)] and the pink oxide staining at station 2 [Fig. 6(a)], which may be slightly overrepresented in the classification image.

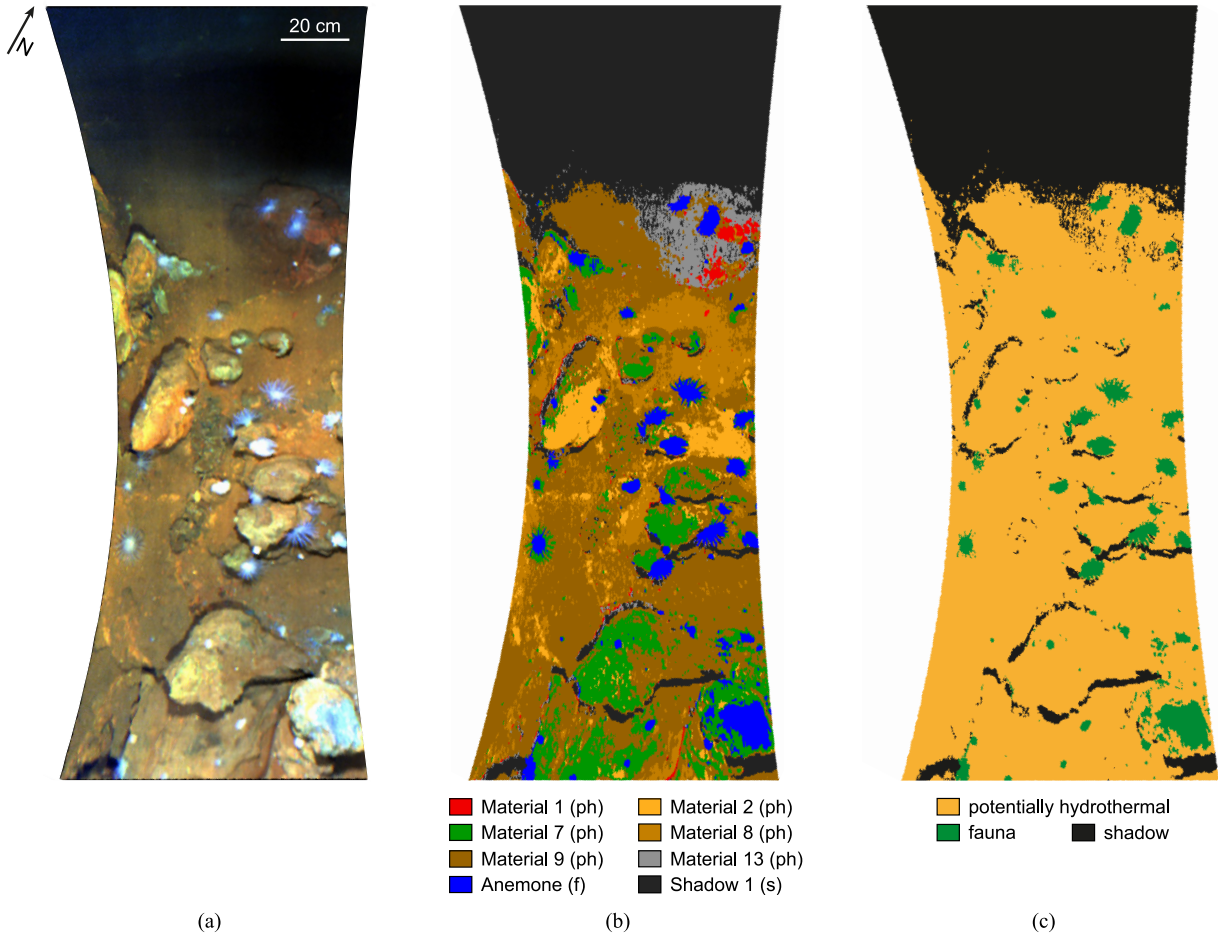


Fig. 5. UHI data and interpretations for station 3 on TAG Mound [location shown in Fig. 1(c)]. (a) Geocorrected pseudo-reflectance data in pseudo-RGB, showing multiple relict chimneys with oxide staining and anemones. The shadow at the top was caused by the housing of the starboard HyBIS lamp. (b) SVM classification result. Material names are those used in the preliminary spectral library in Table I. (c) Interpretation of the classification result showing the distribution of potentially hydrothermal materials, benthic fauna, and shadows. ph = potentially hydrothermal, f = fauna, and s = shadow.

Based on the comparisons of the SVM images and the UHI pseudo-RGB images, as well as results from a previous study using the same UHI and SVM classification [26], the accuracy of the SVM results was estimated to about 90%. Especially, the central parts of the tracks where the spatial resolution was highest yielded relatively accurate classification results.

2) Spectral Database: Due to the lack of ground-truthing information, most of the spectrally distinct materials indicated by the spectral classification results could not be identified. The exceptions were the anemones [stations 3 and 4; Figs. 4(b) and 5(a)] and the copper chloride mineral atacamite [station 4; Fig. 4(b)], which was confirmed during the cruise [65]. It was assumed that the other spectrally distinct materials also represent geologically different materials, but without material identifications, this assumption could not be confirmed.

Analysis of the 48 ROI mean spectra revealed nine groups of two or more similar spectra, suggesting that the same materials may be present at different stations. Mean spectra for two examples, the orange oxide staining and red-brown sediment, are shown in Fig. 7(a). Both of these spectrally distinct materials occurred at stations 3 and 4 on TAG Mound. In addition, sediment with spectral characteristics matching

those from stations 3 and 4 was also found at station 11 on Southern Mound.

A spectral database was created by averaging of similar spectra, including two types of shadow spectra, and combining the averaged spectra with additional spectra observed at only one station. The resulting database contained 26 endmember spectra (Table I). Of these, 24 represented spectrally different materials in the TAG area: 23 were associated with geological surface materials and one with anemones. Examples are shown in Fig. 7(b). In addition, two spectra represented shadows. Although shadow spectra would normally not be included in a spectral database for surface materials, they were included here as they were required for spectral classification.

Based on appearance in the UHI pseudo-RGB data, the HyBIS video data, and information on surface materials from rock samples taken at other locations in the TAG area [54], [65], the 26 endmembers were tentatively divided into the categories “potentially hydrothermal,” “potentially non-hydrothermal,” “fauna,” and “shadow.” Category “potentially hydrothermal” contained 14 endmember spectra, including the confirmed atacamite (Table I). The other endmembers

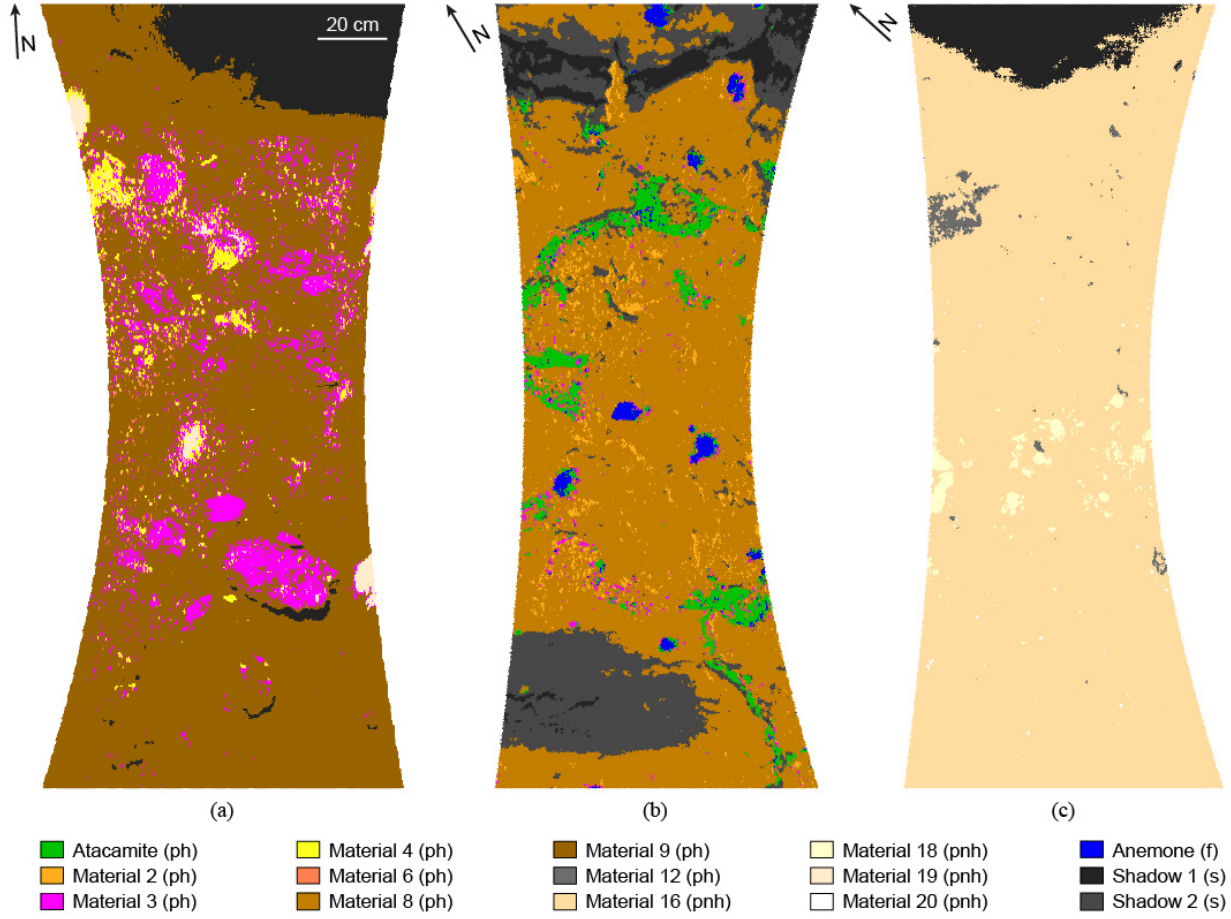


Fig. 6. SVM classification results for the stations in Fig. 4. (a) Station 2. (b) Station 4. (c) Station 6. Material names are those used in the preliminary spectral library in Table I. ph = potentially hydrothermal, pnh = potentially non-hydrothermal, f = fauna, and s = shadow.

were mostly associated with different oxide stains observed, e.g., at stations 2 and 3 [Figs. 4(a) and (b) and 5(a)] and darker sediments that may have some hydrothermal content (Table I). Category “potentially non-hydrothermal” represented pelagic sediments on Southern Mound and at station 1, as well as the chemically altered sediment underneath the bacterial mats at station 9 (Table I).

Coverage estimations for the four categories varied by station. For the potentially hydrothermal category, coverage of the imaged areas varied between less than 1% (station 1) to almost 90% (station 2) (Fig. 8), with 64.4% at station 3 [Fig. 5(c)]. Coverage by the potentially non-hydrothermal category ranged from 0% (stations 3 and 4) to >90% (station 6), whereas fauna were only present at stations 3 [4.3%; Fig. 5(c)] and 4 (1.5%) (Fig. 8). The amounts of shadowed areas were in the range of 7.5%–51.5%.

The coverages shown in Fig. 8 also indicated differences between the stations on TAG Mound (stations 2–4) and those on Southern Mound. At TAG Mound, about 76% of the imaged areas represented potentially hydrothermal material, while non-hydrothermal material constituted less than 1%. In contrast, only about 24% of the seafloor at the Southern Mound stations was considered potentially hydrothermal, while 47% was non-hydrothermal.

V. DISCUSSION

A. Advantages and Disadvantages of a Stationary UHI Platform

The UHI-HyBIS configuration had the advantage of being more stable than a moving platform. By swinging the UHI from side to side, while HyBIS was stationary on the seafloor, relatively well controlled UHI motion was achieved. This motion was free from variations in roll or heading that would inevitably occur when using a moving platform such as an ROV or AUV. Variations in vehicle attitude may lead to distortions in the image, especially in across-track direction, resulting in a lower spatial resolution that can also influence spectral classification [62]. Without such variations, the overall data quality and spatial resolution of the UHI data in this study are higher than for previous UHI data sets [24]–[26].

The changing altitude was a challenge to data processing as it resulted in a systematic change in distance to the seafloor of both the UHI and the lamps, thus changing the illumination field along the track. In previous studies using ROVs [24]–[26], the altitude was generally kept constant to avoid changes in illumination conditions along the track. Correcting for the altitude changes therefore required a new

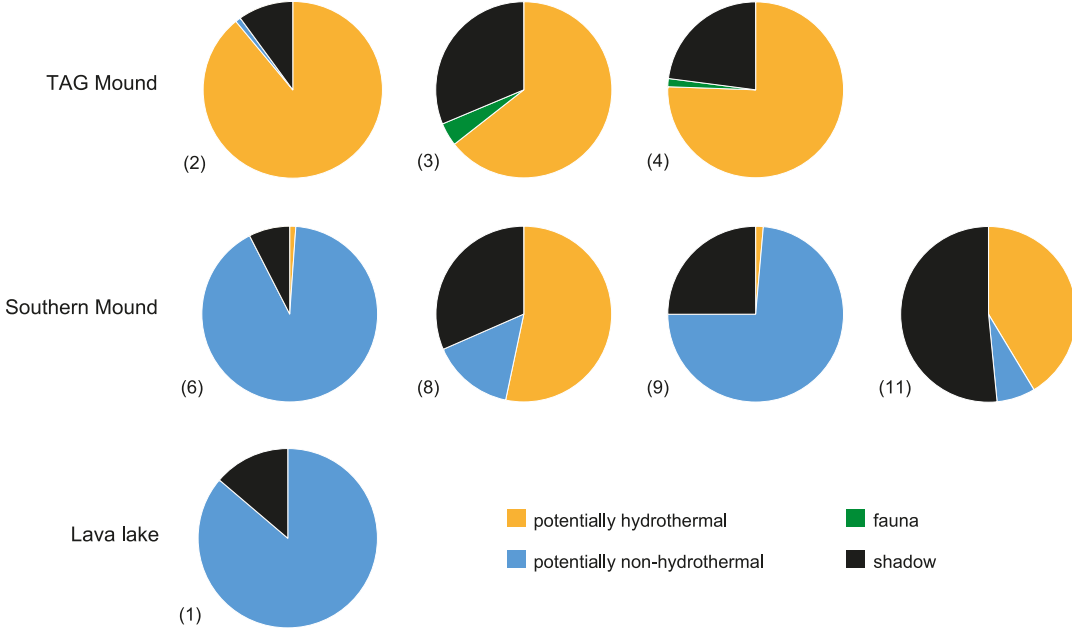


Fig. 8. Relative coverage of potentially hydrothermal materials, potentially non-hydrothermal materials, benthic fauna, and shadows at the different UHI stations (indicated by numbers in brackets).

processing approach, which was complicated by the absence of altitude measurements, swinging angle measurements, and an illumination reference, all of which had to be approximated.

We therefore suggest that continuous measurements of the UHI altitude and the swinging angle should be done during UHI data acquisition on a landed platform. It would also be essential to obtain an illumination reference in order to correct the data to reflectance. In simple acquisition settings (e.g., point measurements), this reference can be obtained from a Spectralon reference standard. To obtain reflectance, the radiance spectrum is divided by the reference spectrum from the Spectralon standard [23], [25], [58]. In more complex acquisition settings involving data acquisition along a survey track, obtaining an illumination reference is not trivial as variations in sensor altitude, pitch, roll, and heading all influence the light field and thus have to be taken into account. In the case of acquisition on HyBIS, seafloor illumination varied both across and along the survey track, due to the lamps illuminating mostly the central portion of the track, and the distance to the seafloor changing with the swinging angle. An illumination reference would therefore have to be obtained for each swinging angle and across the entire track. This could not be realized during data acquisition and therefore an illumination reference was not obtained.

Another setup-induced disadvantage was the imaging of the lower part of the HyBIS frame. As this part of the track had to be cutoff, not the full swath width was available for further analysis and classification. However, the loss of information was not considered high, given that most of the removed image areas did not appear to contain any additional materials not present in the main part of the track. To avoid imaging the frame, the UHI would have had to be mounted at some distance from it, as the UHI's viewing angle of 60° is fixed.

Such a mounting setup was not possible and would not only have compromised platform stability, but also put the UHI at greater risk of damage during launch, landing, and recovery operations.

A major problem during acquisition was the finding of suitable landing spots in the TAG area. The terrain was generally steep and characterized either by an abundance of rocky material (e.g., at and around TAG Mound) or by thick, soft pelagic sediments (e.g., on Southern Mound). In the UHI configuration, HyBIS had a relatively high center of gravity that made it prone to tilting on steeper slopes, and as a result, the seafloor conditions often made it impossible to land HyBIS on the seafloor. We therefore recommend that a stationary UHI platform should be preferably used in flat areas.

Due to the small seafloor coverage of only a few m², a landed platform is mostly suitable for small-scale, detailed studies, e.g., at previously selected targets within a larger and relatively flat area. As the UHI method is also well suited for mapping seabed fauna [23]–[26], [66], UHI measurements using a landed platform may also be applied in habitat mapping, e.g., as high-resolution control measurements within areas previously mapped with lower resolution systems.

B. Evaluation of the Data Analysis Procedure

Of the 12 UHI stations, eight yielded good processing results, showing that the median spectra approach that was applied in the absence of an illumination reference worked well in general. The fact that this approach resulted in pseudo-reflectance data that still contained residual illumination influences, rather than the true reflectance data, was not an issue for spectral classification using the SVM method. However, future studies should focus on obtaining an illumination reference in order to process the UHI data to reflectance.

TABLE I
SUMMARY OF THE PRELIMINARY SPECTRAL LIBRARY FOR THE TAG AREA

Spectra (color in UHI pseudo-RGB)	Interpretation ^a	Stations
Potentially hydrothermal:		
Atacamite (green-blue)	Atacamite	4
Material 1 (red)	Oxide coating or stain	3, 9, 11
Material 2 (orange)	Oxide coating or stain	3, 4
Material 3 (pink)	Oxide coating or stain	2, 4
Material 4 (yellow)	Oxide coating or stain	2, 11
Material 5 (yellow)	Oxide coating or stain	8
Material 6 (red-orange)	Oxide coating or stain	2
Material 7 (green)	Oxide coating or stain	3
Material 8 (brown-red)	Sediment with hydrothermal content	3, 4, 11
Material 9 (brown)	Sediment with hydrothermal content	2, 3
Material 10 (red)	Sediment with hydrothermal content	8
Material 11 (orange)	Sediment with hydrothermal content	1
Material 12 (black)	Hydrothermal crust	6
Material 13 (brown)	Hydrothermal rock?	3
Potentially non-hydrothermal:		
Material 14 (yellow-orange)	Chemically altered sediment underneath (blown-away) bacterial mat	9
Materials 15-18 (beige)	Pelagic sediment	1, 6, 9
Materials 19-20 (light beige)	Potentially deeper sediment exposed by bioturbation, currents or HyBIS feet	1, 2, 6, 8
Materials 21-22 (white)	Sediment dust, probably in water column	8, 11
Fauna:		
Anemone (white-blue)	Anemone	3, 4
Shadow:		
Shadow 1	Shadowed seafloor	2, 3, 4, 6, 8, 9, 11
Shadow 2	Shadowed seafloor	1, 4, 11

^a based on visual interpretation of video data and UHI pseudo-RGB data.

For data processing, the following assumptions were made: 1) the rate of change of the swinging angle is constant along the track; 2) each track represents a full 80° swing from -40° to +40°; and 3) the seafloor is flat relative to HyBIS. In case these assumptions did not hold, processing results and potentially classification results may have been influenced.

Assumption 1 was thought to apply to most stations, as the UHI motion seemed generally smooth. However, a slope in or opposite to the track direction may have influenced UHI motion, with the UHI swinging faster on a negative slope. Slope angles and directions varied at the different stations, but as the UHI's swinging angle was not measured, it is unknown how UHI motion was affected. In general, the difference in line numbers per track at different stations suggests that UHI motion was not uniform and thus may not have been completely smooth along the track.

The UHI likely reached the full 40° at the end of a swing, but the swing may not always have started at -40°. Therefore, assumption 2 may not have applied to all stations. Before the start of a swing, the UHI was held in the -40° position by the hydraulics of the swinging bracket, but it may have slid back slowly a few degrees on its own weight before the swing started. A slope in the track direction would also have promoted sliding back of the UHI.

In general, assumptions 1 and 2 would not have been necessary if the UHI angle had been measured during data

acquisition. In case these assumptions did not hold, this would have influenced geocorrection of the UHI data, i.e., the spatial relationships of the image pixels. The classification of the pixel spectra, however, would have been unaffected.

Assumption 3 was generally true for UHI stations that featured mostly smooth sediments (e.g., stations 6 and 7), but not for stations characterized by rocks or relict chimneys (e.g., stations 3, 5, and 11). Assumption 3 had to be made because the altitude along the survey track was not measured. Where the seafloor was not flat, elevated seafloor areas were closer to the lamps, which resulted in brighter illumination of these areas. During along-track intensity normalization, these areas were overcorrected because their calculated distance to the seafloor was higher than in reality. Consequently, rocks and other elevated features may appear brighter than other areas of the same material, which had to be taken into account for spectral classification. For example, these brighter areas needed to be included in the ROIs to avoid misclassification.

C. Spectrally Different Surface Materials in the TAG Area

The UHI data show a variety of spectrally different materials in the TAG area, both at the active TAG Mound and the inactive Southern Mound. Unfortunately, it was not possible to identify most of the spectrally different materials. Material identification would have required seafloor samples

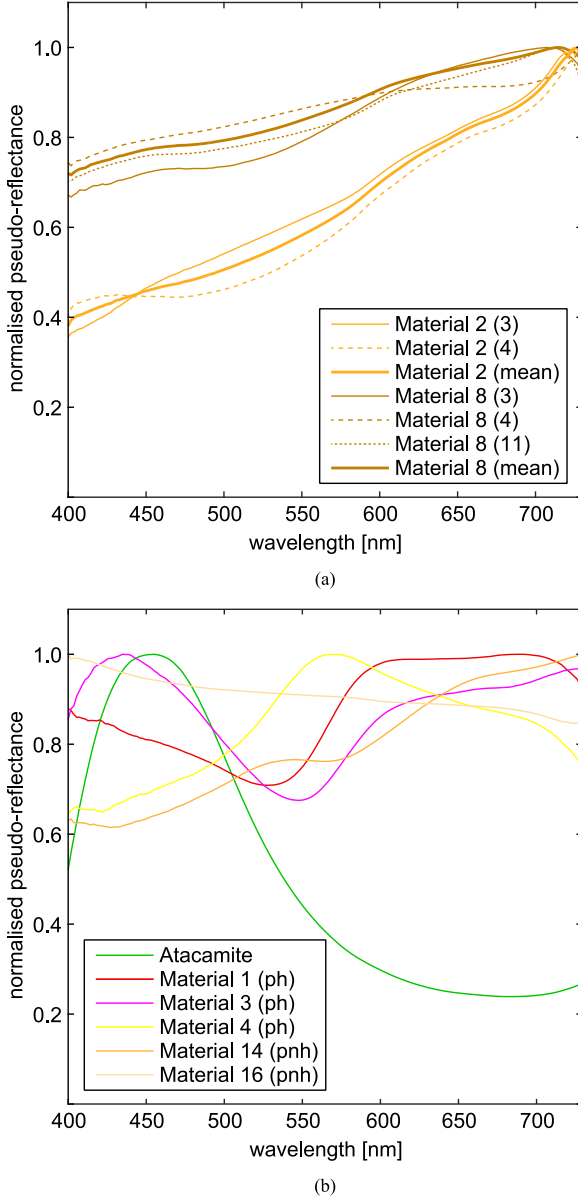


Fig. 7. (a) ROI mean spectra for orange oxide staining (material 2) and brown-red sediment (material 8). Thick lines represent the averaged spectra entered in the preliminary spectral library (Table I). Numbers in brackets indicate the UHI stations. (b) Examples of different endmember spectra normalized to their maximum value. Material names are those used in the preliminary spectral library in Table I. ph = potentially hydrothermal and phn = potentially non-hydrothermal.

from within the scanned areas, but HyBIS could not be equipped with any sampling gear in the UHI configuration. Alternatively, materials could have been identified through comparisons with spectra from existing spectral libraries based on onshore samples, e.g., the United States Geological Survey spectral library [64]. However, these libraries typically focus on the infrared part of the solar spectrum and spectra are given in reflectance, whereas our data contain pseudo-reflectance spectra limited to the visible range, thus making a comparison difficult.

Even without material identifications, it is evident that different types of hydrothermal and non-hydrothermal seafloor

materials occur in the study area. For example, there are likely several types of oxides and sediments with varying hydrothermal contents present at different stations, as shown in the preliminary spectral library in Table I. Without confirmation by ground truthing, however, the material interpretations presented in Table I, as well as the assignments to the “potentially hydrothermal” and “potentially non-hydrothermal” categories, have to be seen as first approximations that require verification.

Similarly, the distribution of the different categories [Figs. 5(c) and 8] is at present only a rough estimate of the true distribution of hydrothermal and non-hydrothermal materials on TAG Mound and Southern Mound. In this context, it is also important to consider the image areas covered by shadows, as it is unclear whether these represent hydrothermal or non-hydrothermal materials, or a combination of both. Consequently, the shadow areas could possibly change the proportions of hydrothermal and non-hydrothermal materials at the different stations, which in turn would change the general trend at both mounds (76% hydrothermal material at TAG Mound, 47% non-hydrothermal material at Southern Mound), given that the relative dimensions of shadowed areas varied between stations. If more data and ground-truthing information became available, the coverage estimates could be improved.

While the seafloor coverage estimates provide an overview of where hydrothermal materials are likely present, it has to be noted that the UHI method is a surface imaging method and is therefore only able to detect hydrothermal materials exposed at the seafloor. However, in the TAG area and other hydrothermal areas, hydrothermal deposits, including massive sulfides, are not necessarily located at the seafloor but in the subsurface [40], [68], [69]. Detecting buried hydrothermal deposits is not possible with an UHI or other optical techniques, and thus requires other geophysical methods such as electromagnetics [70], [71] and seismics [72], [73]. In general, if hyperspectral imaging methods detect hydrothermal material at the seafloor, it is likely that hydrothermal deposits are also present in the subsurface. However, if no or hardly any potentially hydrothermal material exists at the surface, e.g., at station 9 on top of Southern Mound, this does not exclude the presence of deposits in the subsurface.

D. Survey Procedure for Identification of Spectrally Different Materials

To identify the spectrally different materials in the TAG area, more extensive ground-truthing information is required, including seafloor samples from within the areas scanned by the UHI. Samples could not be taken as part of the UHI surveys as HyBIS did not have any sampling equipment when in the UHI configuration. We therefore suggest the following procedure for potential future surveys to ensure material identifications and improvement of the preliminary spectral library in Table I.

As a first step, new UHI data of various hydrothermal and non-hydrothermal materials should be acquired, using a UHI platform with sampling equipment. Survey tracks do not have to be longer than a few meters. Although a stationary platform

might be used in this step, a moving platform would be more suitable for acquisition in the TAG area and other areas with similar terrain conditions. Given that AUVs cannot be used for seafloor sampling, it is recommended to use an ROV as the platform.

It would also be important to acquire the data in a way that allows obtaining an illumination reference to ensure processing the data to true reflectance rather than pseudo-reflectance. Obtaining reflectance data are essential as pseudo-reflectance spectra may not be comparable to data acquired on other platforms, or to existing spectral libraries containing reflectance spectra. An illumination reference could be obtained from light intensity measurements under different angles and subsequent radiative transfer modeling [23], or from a calibrated reference standard such as a Spectralon reference plate [23], [25], [58]. If a reference standard is used on the seafloor, it should cover both the entire length and width of the survey track to account for along-track and across-track variations in vehicle altitude, as these influence the illumination field.

Step 2 involves taking physical samples after each survey track. Samples should include rock material, sediment, and seabed fauna. Sampling could also be done at the UHI stations of this study, but it is preferable that sampling would take place immediately after UHI data acquisition, as surface conditions may change over time.

In step 3, the seafloor samples, and in particular their surface materials, should be identified based on geological and geochemical analyses. The UHI data should then be processed to reflectance (step 4) using the illumination reference.

Step 5 involves setting up a spectral library for the identified materials. The library should be composed of endmember spectra obtained by averaging of pixel spectra from the UHI image at locations where identified samples were taken. Alternatively, endmember spectra could be obtained directly from the samples by conducting hyperspectral measurements in a lab setting. While it might be easier to obtain reflectance data in this case [58], these spectra might differ from those of the survey data due to the different acquisition setup, differences in light output of light sources, and potentially the use of different UHIs. Applying a sample-based spectral library to the survey image data might therefore lead to a poorer classification result.

After step 5, more UHI surveys should be conducted in the study area. Once the data are processed to reflectance, the spectral library can be applied to provide both seafloor classification and identification of seafloor materials. In case steps 3 and 4 could be done onboard, the spectral library could be set up after a first exploratory UHI survey and then used for a more automated classification of UHI data from subsequent surveys. These surveys could also be conducted using an AUV to cover larger areas.

If necessary, the spectral library could be extended as more UHI surveys are conducted. Based on the material identifications, the present coverage estimates for hydrothermal and non-hydrothermal materials should be revised to provide a more reliable overview of the distribution of these materials at the studied locations.

VI. CONCLUSION

In this study, UHI data were acquired at 12 locations in the TAG hydrothermal field at the Mid-Atlantic Ridge, using an UHI on a stationary seafloor platform. Although landing the platform on the seafloor was challenging due to the complex terrain, the acquired data are of high spectral and spatial resolution and provide very stable images and distinct optical fingerprints of OOI on the seafloor. Based on spectral analyses and supervised classification using the SVM method, 24 spectrally different materials were inferred for the studied sites. Due to lack of ground-truthing and seafloor samples, it was unfortunately not possible to identify most of these materials. However, the variety of spectrally different materials in the study area indicates the presence of different types of hydrothermal and non-hydrothermal surface materials.

These results show that the UHI surveys are generally capable of detecting different types of seafloor materials in hydrothermal areas. Combined with appropriate ground truthing, UHI would therefore be well suited for high-resolution mapping and characterization of surface materials on small spatial scales, i.e., a few m² for a stationary UHI platform and several 100 m² for a moving platform. In addition, UHI measurements represent a promising method for habitat mapping and environmental assessments, which will be essential before and after seabed mining operations [46]–[50].

ACKNOWLEDGMENT

The authors would like to thank F. Volden, S. M. Nornes, D. Edge, and R. Locke for their technical support with data acquisition. They would like to thank Captain J. M. Gwinnell and the crew of RRS James Cook for their excellent support at sea. They would also like to thank L. Martin Sandvik Aas (Ecotone AS) for discussions of data analysis and the associate editor and two anonymous reviewers for their constructive comments, which helped to improve this paper.

REFERENCES

- [1] A. F. H. Goetz, G. Vane, J. E. Solomon, and B. N. Rock, “Imaging spectrometry for earth remote sensing,” *Science*, vol. 228, no. 4704, pp. 1147–1153, 1985, doi: [10.1126/science.228.4704.1147](https://doi.org/10.1126/science.228.4704.1147).
- [2] P. Bierwirth, R. Blewett, and D. Huston, “Finding new mineral prospects with HYMAP: Early results from a hyperspectral remote-sensing case study in the west Pilbara,” *AGSO Res. Newslett.*, vol. 31, pp. 1–3, Nov. 1999.
- [3] F. A. Kruse *et al.*, “The spectral image processing system (SIPS)—Interactive visualization and analysis of imaging spectrometer data,” *Remote Sens. Environ.*, vol. 44, nos. 2–3, pp. 145–163, May/Jun. 1993, doi: [10.1016/0034-4257\(93\)90013-N](https://doi.org/10.1016/0034-4257(93)90013-N).
- [4] P. Geladi, J. Burger, and T. Lestander, “Hyperspectral imaging: Calibration problems and solutions,” *Chemometrics Intell. Lab. Syst.*, vol. 72, no. 2, pp. 209–217, Jul. 2004, doi: [10.1016/j.chemolab.2004.01.023](https://doi.org/10.1016/j.chemolab.2004.01.023).
- [5] R. N. Clark *et al.*, “Imaging spectroscopy: Earth and planetary remote sensing with the USGS Tetracorder and expert systems,” *J. Geophys. Res. Planets*, vol. 108, no. E12, Dec. 2003, Art. no. 5131, doi: [10.1029/2002JE001847](https://doi.org/10.1029/2002JE001847).
- [6] F. A. Kruse, J. W. Boardman, and J. F. Huntington, “Comparison of airborne hyperspectral data and EO-1 Hyperion for mineral mapping,” *IEEE Trans. Geosci. Remote Sens.*, vol. 41, no. 6, pp. 1388–1400, Jun. 2003, doi: [10.1109/TGRS.2003.812908](https://doi.org/10.1109/TGRS.2003.812908).
- [7] R. G. Resmini, M. E. Kappus, W. S. Aldrich, J. C. Harsanyi, and M. Anderson, “Mineral mapping with HYperspectral Digital Imagery Collection Experiment (HYDICE) sensor data at Cuprite, Nevada, U.S.A.,” *Int. J. Remote Sens.*, vol. 18, no. 7, pp. 1553–1570, 1997, doi: [10.1080/014311697218278](https://doi.org/10.1080/014311697218278).

- [8] E. Adam, O. Mutanga, and D. Rugege, "Multispectral and hyperspectral remote sensing for identification and mapping of wetland vegetation: A review," *Wetlands Ecol. Manage.*, vol. 18, no. 3, pp. 281–296, 2010, doi: [10.1007/s11273-009-9169-z](https://doi.org/10.1007/s11273-009-9169-z).
- [9] T. Landmann *et al.*, "Application of hyperspectral remote sensing for flower mapping in African savannas," *Remote Sens. Environ.*, vol. 166, pp. 50–60, Sep. 2015, doi: [10.1016/j.rse.2015.06.006](https://doi.org/10.1016/j.rse.2015.06.006).
- [10] S. Roessner, K. Segl, U. Heiden, and H. Kaufmann, "Automated differentiation of urban surfaces based on airborne hyperspectral imagery," *IEEE Trans. Geosci. Remote Sens.*, vol. 39, no. 7, pp. 1525–1532, Jul. 2001, doi: [10.1109/36.934082](https://doi.org/10.1109/36.934082).
- [11] F. Dell'Acqua, P. Gamba, A. Ferrari, J. A. Palmason, J. A. Benediktsson, and K. Arnason, "Exploiting spectral and spatial information in hyperspectral urban data with high resolution," *IEEE Geosci. Remote Sens. Lett.*, vol. 1, no. 4, pp. 322–326, Oct. 2004, doi: [10.1109/LGRS.2004.837009](https://doi.org/10.1109/LGRS.2004.837009).
- [12] A. P. Crósta, C. Sabine, and J. V. Taranik, "Hydrothermal alteration mapping at Bodie, California, using AVIRIS hyperspectral data," *Remote Sens. Environ.*, vol. 65, no. 3, pp. 309–319, Sep. 1998, doi: [10.1016/S0034-4257\(98\)00040-6](https://doi.org/10.1016/S0034-4257(98)00040-6).
- [13] F. F. Sabins, "Remote sensing for mineral exploration," *Ore Geol. Rev.*, vol. 14, nos. 3–4, pp. 157–183, Sep. 1999, doi: [10.1016/S0169-1368\(99\)00007-4](https://doi.org/10.1016/S0169-1368(99)00007-4).
- [14] R. N. Clark, T. V. V. King, M. Klejwa, G. A. Swayze, and N. Vergo, "High spectral resolution reflectance spectroscopy of minerals," *J. Geophys. Res. Solid Earth*, vol. 95, no. B8, pp. 12653–12680, Aug. 1990, doi: [10.1029/JB095iB08p12653](https://doi.org/10.1029/JB095iB08p12653).
- [15] F. D. van der Meer *et al.*, "Multi- and hyperspectral geologic remote sensing: A review," *Int. J. Appl. Earth Observ. Geoinformation*, vol. 14, no. 1, pp. 112–128, Feb. 2012, doi: [10.1016/j.jag.2011.08.002](https://doi.org/10.1016/j.jag.2011.08.002).
- [16] W. M. Klonowski, P. R. C. S. Fearn, and M. J. Lynch, "Retrieving key benthic cover types and bathymetry from hyperspectral imagery," *J. Appl. Remote Sens.*, vol. 1, no. 1, p. 011505, Jan. 2007, doi: [10.1117/1.2816113](https://doi.org/10.1117/1.2816113).
- [17] P. R. C. Fearn, W. Klonowski, R. C. Babcock, P. England, and J. Phillips, "Shallow water substrate mapping using hyperspectral remote sensing," *Cont. Shelf Res.*, vol. 31, no. 12, pp. 1249–1259, Aug. 2011, doi: [10.1016/j.csr.2011.04.005](https://doi.org/10.1016/j.csr.2011.04.005).
- [18] H. M. Dierssen, "Overview of hyperspectral remote sensing for mapping marine benthic habitats from airborne and underwater sensors," in *Proc. SPIE*, vol. 8870, p. 7, Sep. 2013, doi: [10.1117/12.2026529](https://doi.org/10.1117/12.2026529).
- [19] H. M. Dierssen, A. Chlus, and B. Russell, "Hyperspectral discrimination of floating mats of seagrass wrack and the macroalgae Sargassum in coastal waters of Greater Florida Bay using airborne remote sensing," *Remote Sens. Environ.*, vol. 167, pp. 247–258, Sep. 2015, doi: [10.1016/j.rse.2015.01.027](https://doi.org/10.1016/j.rse.2015.01.027).
- [20] Z. Volent, G. Johnsen, and F. Sigernes, "Kelp forest mapping by use of airborne hyperspectral imager," *J. Appl. Remote Sens.*, vol. 1, no. 1, p. 011503, Dec. 2007, doi: [10.1117/1.2822611](https://doi.org/10.1117/1.2822611).
- [21] G. Johnsen, "Underwater hyperspectral imaging," U.S. Patent 8 502 974 B2, Aug. 6, 2013.
- [22] G. Johnsen, "Underwater hyperspectral imaging," U.S. Patent 8 767 205 B2, Jul. 1, 2014.
- [23] G. Johnsen *et al.*, "Underwater hyperspectral imagery to create biogeochemical maps of seafloor properties," in *Subsea Optics and Imaging*, J. Watson and O. Zielinski, Eds., Cambridge, U.K.: Woodhead, 2013, ch. 20, pp. 508–535.
- [24] J. Tegdan *et al.*, "Underwater hyperspectral imaging for environmental mapping and monitoring of seabed habitats," in *Proc. OCEANS*, Genoa, Italy, May 2015, pp. 1–6, doi: [10.1109/OCEANS-Genova.2015.7271703](https://doi.org/10.1109/OCEANS-Genova.2015.7271703).
- [25] G. Johnsen, M. Ludvigsen, A. Sørensen, and L. M. S. Aas, "The use of underwater hyperspectral imaging deployed on remotely operated vehicles—Methods and applications," *IFAC-PapersOnLine*, vol. 49, no. 23, pp. 476–481, 2016, doi: [10.1016/j.ifacol.2016.10.451](https://doi.org/10.1016/j.ifacol.2016.10.451).
- [26] I. Dumke *et al.*, "First hyperspectral imaging survey of the deep seafloor: High-resolution mapping of manganese nodules," *Remote Sens. Environ.*, vol. 209, pp. 19–30, May 2018, doi: [10.1016/j.rse.2018.02.024](https://doi.org/10.1016/j.rse.2018.02.024).
- [27] A. A. Mogstad and G. Johnsen, "Spectral characteristics of coralline algae: A multi-instrumental approach, with emphasis on underwater hyperspectral imaging," *Appl. Opt.*, vol. 56, no. 36, pp. 9957–9975, Dec. 2017, doi: [10.1364/AO.56.009957](https://doi.org/10.1364/AO.56.009957).
- [28] Ø. Sture, M. Ludvigsen, F. Sørøide, and L. M. S. Aas, "Autonomous underwater vehicles as a platform for underwater hyperspectral imaging," in *Proc. OCEANS*, Aberdeen, U.K., Jun. 2017, pp. 1–8, doi: [10.1109/OCEANSE.2017.8084995](https://doi.org/10.1109/OCEANSE.2017.8084995).
- [29] S. D. Scott, "Deep ocean mining," *Geosci. Canada*, vol. 28, no. 2, pp. 87–96, Jun. 2001.
- [30] G. P. Glasby, "Deep seabed mining: Past failures and future prospects," *Mar. Georesources Geotechnology*, vol. 20, no. 2, pp. 161–176, 2002, doi: [10.1080/03608860290051859](https://doi.org/10.1080/03608860290051859).
- [31] P. A. Rona, "Resources of the sea floor," *Science*, vol. 299, no. 5607, pp. 673–674, Jan. 2003, doi: [10.1126/science.1080679](https://doi.org/10.1126/science.1080679).
- [32] Y. Beaudoin, A. Bredbenner, and E. Baker, "Wealth in the Oceans: Deep sea mining on the horizon?" *Environ. Dev.*, vol. 12, pp. 50–61, Oct. 2014, doi: [10.1016/j.envdev.2014.07.001](https://doi.org/10.1016/j.envdev.2014.07.001).
- [33] S. E. Beaulieu, T. E. Graedel, and M. D. Hannington, "Should we mine the deep seafloor?" *Earth's Future*, vol. 5, no. 7, pp. 655–658, Jul. 2017, doi: [10.1002/2017EF000605](https://doi.org/10.1002/2017EF000605).
- [34] P. Hoagland *et al.*, "Deep-sea mining of seafloor massive sulfides," *Mar. Policy*, vol. 34, no. 3, pp. 728–732, May 2010, doi: [10.1016/j.marpol.2009.12.001](https://doi.org/10.1016/j.marpol.2009.12.001).
- [35] M. D. Hannington, J. Jamieson, T. Monecke, S. Petersen, and S. Beaulieu, "The abundance of massive sulfide deposits," *Geology*, vol. 39, no. 12, pp. 1155–1158, Dec. 2011, doi: [10.1130/G32468.1](https://doi.org/10.1130/G32468.1).
- [36] A. R. Miller *et al.*, "Hot brines and recent iron deposits in deeps of the Red Sea," *Geochimica Cosmochimica Acta*, vol. 30, no. 3, pp. 341–359, Mar. 1966, doi: [10.1016/0016-7037\(66\)90007-X](https://doi.org/10.1016/0016-7037(66)90007-X).
- [37] J. Francheteau *et al.*, "Massive deep-sea sulphide ore deposits discovered on the East Pacific Rise," *Nature*, vol. 277, no. 5697, pp. 523–528, Feb. 1979, doi: [10.1038/277523a0](https://doi.org/10.1038/277523a0).
- [38] G. Cherkashov *et al.*, "Two new hydrothermal fields at the Mid-Atlantic Ridge," *Mar. Georesources Geotechnology*, vol. 26, no. 4, pp. 308–316, Dec. 2008, doi: [10.1080/10641190802400708](https://doi.org/10.1080/10641190802400708).
- [39] P. A. Rona, G. Klinkhammer, T. A. Nelsen, J. H. Trefry, and H. Elderfield, "Black smokers, massive sulphides and vent biota at the Mid-Atlantic Ridge," *Nature*, vol. 321, no. 6065, pp. 33–37, May 1986, doi: [10.1038/321033a0](https://doi.org/10.1038/321033a0).
- [40] P. A. Rona *et al.*, "Relict hydrothermal zones in the TAG hydrothermal field, Mid-Atlantic Ridge 26°N, 45°W," *J. Geophys. Res. Solid Earth*, vol. 98, no. B6, pp. 9715–9730, Jun. 1993, doi: [10.1029/93JB00552](https://doi.org/10.1029/93JB00552).
- [41] P. A. Rona *et al.*, "Heat flow and mineralogy of TAG relict high-temperature hydrothermal zones: Mid-Atlantic Ridge 26°N, 45°W," *Geophys. Res. Lett.*, vol. 23, no. 23, pp. 3507–3510, Nov. 1996, doi: [10.1029/96GL03257](https://doi.org/10.1029/96GL03257).
- [42] M. D. Hannington, G. Thompson, P. A. Rona, and S. D. Scott, "Gold and native copper in supergene sulphides from the Mid-Atlantic Ridge," *Nature*, vol. 33, no. 6168, pp. 64–66, May 1988, doi: [10.1038/333064a0](https://doi.org/10.1038/333064a0).
- [43] C.-F. You and M. J. Bickle, "Evolution of an active sea-floor massive sulphide deposit," *Nature*, vol. 394, no. 6694, pp. 668–671, Aug. 1998, doi: [10.1038/29279](https://doi.org/10.1038/29279).
- [44] R. B. Pedersen *et al.*, "Discovery of a black smoker vent field and vent fauna at the Arctic Mid-Ocean Ridge," *Nature Commun.*, vol. 1, Nov. 2010, Art. no. 126, doi: [10.1038/ncomms1124](https://doi.org/10.1038/ncomms1124).
- [45] Nautilus Minerals, Vancouver, BC, Canada. (Apr. 14, 2014). *Nautilus Minerals and State of PNG Resolve Issues and Sign Agreement, News Release*. [Online]. Available: http://www.nautilusminerals.com/irm/PDF/1144_0/NautilusMineralsandStateofPNGResolveIssuesandSignA
- [46] C. Lee Van Dover, "Mining seafloor massive sulphides and biodiversity: What is at risk?" *ICES J. Mar. Sci.*, vol. 68, no. 2, pp. 341–348, Jan. 2011, doi: [10.1093/icesjms/fsq086](https://doi.org/10.1093/icesjms/fsq086).
- [47] *Environmental Management Needs for Exploration and Exploitation of Deep Sea Minerals*, International Seabed Authority, Kingston, Jamaica, 2012.
- [48] R. E. Boschen, A. A. Rowden, M. R. Clark, and J. P. A. Gardner, "Mining of deep-sea seafloor massive sulfides: A review of the deposits, their benthic communities, impacts from mining, regulatory frameworks and management strategies," *Ocean Coastal Manage.*, vol. 84, pp. 54–67, Nov. 2013, doi: [10.1016/j.ocecoaman.2013.07.005](https://doi.org/10.1016/j.ocecoaman.2013.07.005).
- [49] R. E. Boschen, A. A. Rowden, M. R. Clark, A. Pallentin, and J. P. A. Gardner, "Seafloor massive sulfide deposits support unique megafaunal assemblages: Implications for seabed mining and conservation," *Mar. Environ. Res.*, vol. 115, pp. 78–88, Apr. 2016, doi: [10.1016/j.marenres.2016.02.005](https://doi.org/10.1016/j.marenres.2016.02.005).
- [50] J. M. Durden *et al.*, "A procedural framework for robust environmental management of deep-sea mining projects using a conceptual model," *Mar. Policy*, vol. 84, pp. 193–201, Oct. 2017, doi: [10.1016/j.marpol.2017.07.002](https://doi.org/10.1016/j.marpol.2017.07.002).
- [51] S. E. Humphris *et al.*, "The internal structure of an active sea-floor massive sulphide deposit," *Nature*, vol. 377, no. 6551, pp. 713–716, Oct. 1995, doi: [10.1038/37713a0](https://doi.org/10.1038/37713a0).

- [52] S. E. Humphris, M. K. Tivey, and M. A. Tivey, "The Trans-Atlantic Geotraverse hydrothermal field: A hydrothermal system on an active detachment fault," *Deep Sea Res. II, Top. Studies Oceanogr.*, vol. 121, pp. 8–16, Nov. 2015, doi: [10.1016/j.dsr2.2015.02.015](https://doi.org/10.1016/j.dsr2.2015.02.015).
- [53] P. Bird, "An updated digital model of plate boundaries," *Geochem., Geophys., Geosyst.*, vol. 4, no. 3, Mar. 2003, Art. no. 1027, doi: [10.1029/2001GC000252](https://doi.org/10.1029/2001GC000252).
- [54] S. Petersen, "RV METEOR fahrtbericht/cruise report M127 metal fluxes and resource potential at the slow-spreading TAG mid-ocean ridge segment (26°N, MAR)—Blue Mining@Sea," GEOMAR Helmholtz Centre Ocean Res. Kiel, Kiel, Germany, GEOMAR Rep. 032, Nov. 2016.
- [55] M. D. Hannington, A. G. Galley, P. M. Herzig, and S. Petersen, "Comparison of the TAG mound and stockwork complex with Cyprus type massive sulfide deposits," in *Proc. Ocean Drill. Program Sci. Results*, vol. 158, May 1998, pp. 389–415, doi: [10.2973/odp.proc.sr.158.217.1998](https://doi.org/10.2973/odp.proc.sr.158.217.1998).
- [56] C. Lalou, J.-L. Reyss, E. Brichet, P. A. Rona, and G. Thompson, "Hydrothermal activity on a 10⁵-year scale at a slow-spreading ridge, TAG hydrothermal field, Mid-Atlantic Ridge 26°N," *J. Geophys. Res.*, vol. 100, no. B9, pp. 17855–17862, Sep. 1995, doi: [10.1029/95JB01858](https://doi.org/10.1029/95JB01858).
- [57] B. J. Murton and W. Glover, "Surveyor, sampler for deep-ocean operations HyBIS enables interaction with seafloor up to 6,000-meter depths," *Sea Technol.*, vol. 54, no. 6, pp. 27–30, Jun. 2013.
- [58] P. A. Letnes *et al.*, "Underwater hyperspectral classification of deep sea corals exposed to a toxic compound," doi: [10.1101/150060](https://doi.org/10.1101/150060). [Online]. Available: <https://www.biorxiv.org/content/early/2018/04/16/150060>.
- [59] G. Camps-Valls *et al.*, "Robust support vector method for hyperspectral data classification and knowledge discovery," *IEEE Trans. Geosci. Remote Sens.*, vol. 42, no. 7, pp. 1530–1542, Jul. 2004, doi: [10.1109/TGRS.2004.827262](https://doi.org/10.1109/TGRS.2004.827262).
- [60] F. Melgani and L. Bruzzone, "Classification of hyperspectral remote sensing images with support vector machines," *IEEE Trans. Geosci. Remote Sens.*, vol. 42, no. 8, pp. 1778–1790, Aug. 2004, doi: [10.1109/TGRS.2004.831865](https://doi.org/10.1109/TGRS.2004.831865).
- [61] G. Mountrakis, J. Im, and C. Ogole, "Support vector machines in remote sensing: A review," *ISPRS J. Photogramm. Remote Sens.*, vol. 66, no. 3, pp. 247–259, May 2011, doi: [10.1016/j.isprsjprs.2010.11.001](https://doi.org/10.1016/j.isprsjprs.2010.11.001).
- [62] P. Ghamisi, J. Plaza, Y. Chen, J. Li, and A. J. Plaza, "Advanced spectral classifiers for hyperspectral images: A review," *IEEE Geosci. Remote Sens. Mag.*, vol. 5, no. 1, pp. 8–32, Mar. 2017.
- [63] J. M. Bioucas-Dias, A. Plaza, G. Camps-Valls, P. Scheunders, N. M. Nasrabadi, and J. Chanussot, "Hyperspectral remote sensing data analysis and future challenges," *IEEE Geosci. Remote Sens. Mag.*, vol. 1, no. 2, pp. 6–36, Jun. 2013, doi: [10.1109/MGRS.2013.2244672](https://doi.org/10.1109/MGRS.2013.2244672).
- [64] M. Story and R. G. Congalton, "Accuracy assessment: A user's perspective," *Photogramm. Eng. Remote Sens.*, vol. 52, no. 3, pp. 397–399, 1986.
- [65] B. J. Murton, "Cruise report: Expedition JC 138: 29th June–8th August 2016, Mid Atlantic Ridge, 26° 8.38'N; 44° 49.92'W," Nat. Oceanogr. Centre, Southampton, U.K., 2018.
- [66] I. Dumke *et al.*, "Underwater hyperspectral imaging as an *in situ* taxonomic tool for deep-sea megafauna," *Sci. Rep.*, vol. 8, Sep. 2018, Art. no. 12860.
- [67] R. N. Clark *et al.* (2007). USGS Digital Spectral Library Splib06a. U.S. Geological Survey, Digital Data Series 231. [Online]. Available: <http://speclab.cr.usgs.gov/spectral.lib06>
- [68] M. Minniti and F. F. Bonavia, "Copper-ore grade hydrothermal mineralization discovered in a seamount in the Tyrrhenian Sea (Mediterranean): Is the mineralization related to porphyry-coppers or to base metal lodes?" *Mar. Geol.*, vol. 59, nos. 1–4, pp. 271–282, 1984, doi: [10.1016/0025-3227\(84\)90097-5](https://doi.org/10.1016/0025-3227(84)90097-5).
- [69] S. Petersen *et al.*, "Drilling shallow-water massive sulfides at the Palinuro volcanic complex, Aeolian island arc, Italy," *Econ. Geol.*, vol. 109, no. 8, pp. 2129–2158, Dec. 2014, doi: [10.2113/econgeo.109.8.2129](https://doi.org/10.2113/econgeo.109.8.2129).
- [70] P. Queralt, A. G. Jones, and J. Ledo, "Electromagnetic imaging of a complex ore body: 3D forward modeling, sensitivity tests, and down-mine measurements," *Geophysics*, vol. 72, no. 2, pp. F85–F95, Mar. 2007, doi: [10.1190/1.2437105](https://doi.org/10.1190/1.2437105).
- [71] N. Immura, T.-N. oto, J. Takekawa, and H. Mikada, "Application of marine controlled-source electromagnetic sounding to submarine massive sulphides explorations," *SEG Tech. Program Expanded Abstracts*, vol. 2011, pp. 730–734, Jan. 2011, doi: [10.1190/1.3628182](https://doi.org/10.1190/1.3628182).
- [72] B. Milkereit *et al.*, "Seismic imaging of massive sulfide deposits; Part II, reflection seismic profiling," *Econ. Geol.*, vol. 91, no. 5, pp. 829–834, Aug. 1996, doi: [10.2113/gsecongeo.91.5.829](https://doi.org/10.2113/gsecongeo.91.5.829).
- [73] A. Malemir and G. Bellefleur, "3D seismic reflection imaging of volcanic-hosted massive sulfide deposits: Insights from reprocessing Halfmile Lake data, New Brunswick, Canada," *Geophysics*, vol. 74, no. 6, pp. B209–B219, Nov. 2009, doi: [10.1190/1.3230495](https://doi.org/10.1190/1.3230495).

Ines Dumke received the B.Sc., M.Sc., and Ph.D. degrees in geophysics from Kiel University, Kiel, Germany, in 2009, 2012, and 2015, respectively.

In 2010, she joined the University of Otago, Dunedin, New Zealand, as a Study Abroad Student. From 2012 to 2015, she was a Research Assistant at GEOMAR Helmholtz Centre for Ocean Research Kiel, Kiel. From 2015 to 2017, she was a Post-Doctoral Fellow with the Department of Marine Technology, Norwegian University of Science and Technology, Trondheim, Norway. Since 2017, she has been a Post-Doctoral Researcher with GEOMAR Helmholtz Centre for Ocean Research Kiel. Her research interests include optical and acoustic imaging of the seafloor and the subsurface, hyperspectral imaging, image classification, and machine learning.

Dr. Dumke is a member of the European Geosciences Union.

Martin Ludvigsen received the M.Sc. and Ph.D. degrees in marine technology from the Norwegian University of Science and Technology (NTNU), Trondheim, Norway, in 2001 and 2010, respectively.

In 2009, he participated in the startup of the Applied Underwater Laboratory, NTNU, where he has been the Manager. From 2010 to 2014, he was a Post-Doctoral Fellow with the Department of Marine Technology, NTNU. In 2012, he joined the Woods Hole Oceanographic Institution, Woods Hole, MA, USA, as a Guest Investigator on a Fulbright scholarship. Since 2014, he has been a Professor of underwater technology with the Department of Marine Technology, NTNU. In 2015, he was an announced Adjunct Associate Professor of marine technology with the University Centre in Svalbard, Longyearbyen, Svalbard, Norway. In 2015, he was a Co-Founder of the NTNU technology spin-off Blueye robotics where he is currently the CTO of this startup. His research interests include the applications of underwater robotics, cameras, and acoustical instruments.

Steinar L. Ellefmo received the M.Sc. degree in resource geology and the Dr.Ing. (Ph.D. equivalent) degree in technical resource geology from the Norwegian University of Science and Technology (NTNU), Trondheim, Norway, in 1999 and 2005, respectively.

In 2006/2007, he was a Visiting Scholar at the W.H. Bryan Mining & Geology Research Centre (BRC) at the Sustainable Minerals Institute (SMI), Queensland, Australia. From 2007 to 2008, he was a Mine Geologist at North Cape Minerals AS, Norway. From 2009 to 2010, he was a Researcher with the Department of Geoscience and Petroleum, NTNU, where he has been since 2010, he has been an Associate Professor at the Department of Geoscience and Petroleum, NTNU. Since 2013, he has been in the new marine minerals initiative at NTNU within the strategic research area NTNU Oceans. In 2013/2014, he led the work that published the first estimate of the undiscovered mineral resource potential inside the Norwegian jurisdiction along the mid-Atlantic ridge. Since 2014, he has been the Project Manager of the Deep-Sea Mining Pilot Project at NTNU. His research interests include the broad field of mineral resource management, specifically mining engineering, geostatistics, 3-D geometric ore body modeling, and mineral resource potential assessment.

Dr. Ellefmo is a member of the Australasian Institute of Mining and Metallurgy.

Fredrik Søreide received the M.Sc. and Ph.D. degrees in marine technology from the Norwegian University of Science and Technology, Trondheim, Norway, and the M.B.A. degree from Imperial College, London, U.K.

He is currently an Adjunct Professor in underwater technology with the Department of Marine Technology, NTNU. He was the Principal Investigator on the Ormen Lange deepwater archeology project, where he pioneered the use of marine technology in shipwreck investigations. He also designed the robotic system that was the first to dive in the Puerto Rico Trench, the deepest point in the Atlantic Ocean. His research interests include the applications of underwater technology in marine science, particularly deep water archeology, biology and geology, several marine minerals, and ocean mining projects.

Geir Johnsen is currently a Professor in marine biology with the Department of Biology, Centre for Autonomous Operations and Systems, Norwegian University of Technology and Science (NTNU), Trondheim, Norway. He is also a Professor II with the University Centre in Svalbard, Longyearbyen, Svalbard, Norway.

In 1992/1993, he was a Visiting Researcher with the University of California, Santa Barbara, CA, USA. In 2010/2011, he was a Visiting Researcher with Curtin University, Perth, WA, Australia. He is one of the founding partners of the NTNU spin-off company Ecotone. He has authored over 110 articles and a co-editor for the books *Ecosystem Barents Sea* (Tapir Academic Press) and *Phytoplankton pigments: Updates on Characterization, Chemotaxonomy and Applications in Oceanography* (Cambridge University Press, 2011). His research areas include marine ecology and biodiversity, bio-optics, photosynthesis, pigment chemotaxonomy, underwater robotics and sensor development for *in situ* identification, mapping and monitoring of bio-geo-chemical objects of interest in the marine environment.

Bramley J. Murton received the B.Sc. degree in geology from the University of Edinburgh, Edinburgh, U.K., in 1982, and the Ph.D. degree from the Department of Earth Sciences, Open University, Milton Keynes, U.K., in 1986.

He is currently an Associate Head of marine geosciences with the National Oceanography Centre, Southampton, U.K., where he leads the marine minerals research team. He has led numerous research programs including studies of mid-ocean ridge volcanism, hydrothermal activity and seafloor mineralisation.

Dr. Murton was a Chairman of the international consortium for mid-ocean ridge research, InterRidge from 2010 to 2013. He is currently on the executive board of the EC-funded Research and Development Program “Blue Mining” developing technologies for seafloor mineral resource exploration, assessment and extraction. He is also the Chief Scientist for the international research project “MarineE-tech” studying critical elements in ferromanganese-cobalt-rich crusts on the deep Atlantic seafloor. He has a long track record in developing and deploying underwater robotic and autonomous technology for extreme environments, including the HyBIS robotic underwater vehicle.